3D View Reconstruction from Endoscopic Videos for Gastrointestinal Tract Surgery Planning

Xiaohong W. Gao[1][a], Annisa Rahmanti[1][b] and Barbara Braden[2][c]
[1]*Department of Computer Science, Middlesex University, London, U.K.*
[2]*Medical Department B, University of Münster, Germany*

Keywords: Deep Learning, 3D Reconstruction, Nerfs, Gastrointestinal Tract, SfM, 2D Endoscopic Video, Endoscopic Artefacts.

Abstract: This paper investigates the application of neural radiance field (NeRF) to reconstruct a 3D model from 2D endoscopic videos for surgical planning and removal of gastrointestinal lesions. It comprises three stages. The first one is video preprocess to remove frames with artefact of colour misalignment based on a deep learning network. Then the remaining frames are converted into NeRF compatible format. This stage includes extraction of camera information regarding intrinsic, extrinsic and ray pathway parameters as well as conversion to NeRF format based on COLMAP library, a pipeline built upon structure-from-motion (SfM) with multi-view stereo (MVS). Finally the training takes place for establishment of NeRF model implemented upon Nerfstudio library. Initial results illustrate that this end-to-end, i.e. from 2D video input to 3D model output deep learning architecture presents great potentials for reconstruction of gastrointestinal tract. Base on the two sets of data containing 2600 images, the similarity measures of SSIM, PSNR and LPIPS between original (ground truth) and rendered images are 19.46 ± 2.56, 0.70 ± 0.054, and 0.49 ± 0.05 respectively. Future work includes enlarging dataset and removal of ghostly artefact from rendered images.

1 INTRODUCTION

Gastrointestinal tract (GI) cancers (oesophagus, stomach, bowel), were responsible for 26.3% of cancer cases and 35.4% of deaths worldwide in 2018 (Lu 2021). As the 2nd largest death caused by cancer in the world (after lung cancer), GI cancers have very low 5-year survival rate (<20%). At present, the only curative and most effective treatment for early GI cancer or lesion is the removal of concerned lesion endoscopically, especially, for a lesion confined to the mucosal layer, the surface columnar epithelium and the first of four layers on the GI wall. In this procedure, a substance is injected first under the target to act as a cushion. Then a surgical plan by marking cutting lines is conducted. Finally, the dissection takes place at submucosal layer under the concerned lesion following the planning boundary. The key to success of this surgery is that the endoscopists have a clear view of the lesion, the planned lines and surroundings from varying view angles throughout in order to perform precise dissection.

The challenges here are that all the views are confined into a narrow (~2cm in diameter) cylindrical food path or tube where the endoscopic camera travels in one direction, resulting in some concerned tissues, anatomy and planned boundary being invisible. In addition, in this complex surgical scene, the endoscopist/surgeon/clinician has to compete with various motions coming from respiration, heartbeat, camera as well as muscles. Because of this, at present, all these operations can only be conducted by expert endoscopists, which put significant amount of pressure in health care systems. Figure 1 demonstrates the process of resection of a polyp in the stomach endoscopically. While the lesion in Figure 1 is benign, if left untreated, it could progress into cancer. Hence resection is in need. Once the target is confirmed (Figure 1 (a)), an injection of a dedicated substance is carried out to highlight and alleviate the lesion whereby

[a] https://orcid.org/0000-0002-8103-6624
[b] https://orcid.org/0000-0001-9478-6267
[c] https://orcid.org/0000-0002-8534-6873

Gao, X. W., Rahmanti, A. and Braden, B.
3D View Reconstruction from Endoscopic Videos for Gastrointestinal Tract Surgery Planning.
DOI: 10.5220/0013125000003911

In *Proceedings of the 18th International Joint Conference on Biomedical Engineering Systems and Technologies (BIOSTEC 2025) - Volume 1*, pages 221-228
ISBN: 978-989-758-731-3; ISSN: 2184-4305

a surgical planning can be made (Figure 1(b)). Then the lesion can be removed safely (Figure 1(c)).

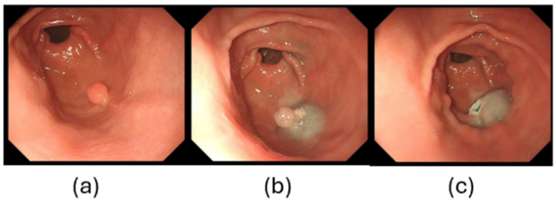

Figure 1: Demonstration of lesion resection endoscopically. (a) a lesion is detected; (b) cushion is injected; (c) successful removal of the concerned lesion.

Hence reconstruction of 3D view of concerned lesions plays an important role in endoscopic surgical planning and lesion removal. 3D reconstruction for GI from endoscopic videos has been studied by a number of researchers. For example, Ali et al (Ali 2021a) has established a physical model of oesophagus that is applied to develop an AI system to quantify Barrett's oesophagus. The researchers as detailed in (Prinzen, 2015) has been established the shape of oesophagus to allow visualization of additional contextual and geometrical information of oesophagus, from panorama image to 3D points cloud then to regular triangulation mesh. Recently, 3D shape reconstruction of whole stomach based on structure-from-motion (SfM) (Widya 2019) is investigated by spreading indigo carmine (IC) dye on the stomach surface to present colour texture of the stomach. This is because endoscopic videos present weak texture of GI surface. On the other hand, the approach of SfM appears to present robust results when it comes 3D reconstruction from 2D videos. Further study for deep multi-view stereo for dense 3D reconstruction (Bae 2020) is also conducted based on SfM and is consisted of 3 steps, which are sparse reconstruction via SfM, monocular depth estimation and embedding vector generation via patch embedding network.

The steps to construct a 3D model from 2D image usually include image collection, feature or/and keypoint detection and extraction, keypoint tracking and matching, structure from motion to determine camera intrinsic, extrinsic and orientation parameters, and key point-cloud reconstruction, such as mesh reconstruction, mesh refinement and mesh texturing.

With the current advances of state-of-the-art (SOTA) deep learning (DL) techniques, many innovative approaches have been developed towards reconstructing 3D deformable objects.

In this study, 3D scene reconstruction based on 2D endoscopic videos is conducted based on SOTA neural radiance field (NeRF) so that a lesion can be viewed from all viewing angles, allowing correct recognition of concerned lesions, tissue types and related anatomy, leading to an assistant system in an operative room allowing multiple views while performing lesion removal.

NeRF (Mildenhall 2020) addresses the long-standing problem in computer vision field, which is to reconstruct a 3D representation of a scene from sparse 2D images. NeRF method synthesizes a new view by directly optimising parameters of a continuous 5D scene representation to minimize the error of rendering a set of captured images. NeRF represents a scene using a fulling connected deep network with an input of a single continuous 5D coordinate (i.e. 3D spatial + 2D view direction angles). The output of this network is the volume density and view-dependent emitted radiance at that spatial location.

2 METHODOLOGY

2.1 Image Pre-Process to Remove Artefact of Colour Misalignment

Due to the confinement of narrow space of GI, it is quite common that as many as a quarter video frames contain several types of artefacts, such as water bubbles, instrument, and saturation. While these artefacts are present most of the time, the concerned image features are still visible. However, the artefact of colour misalignment, where coloured frames of red, green and blue are acquired at different locations because of the combination of movements when an endo camera travels, should be removed not only because most of interested contents are not present but also the presence of these artificial colours will affect the detection of camera light of rays, hence affecting the accuracy of training. Figure 2 illustrates a number of artefacts present in a video clip, where the top row

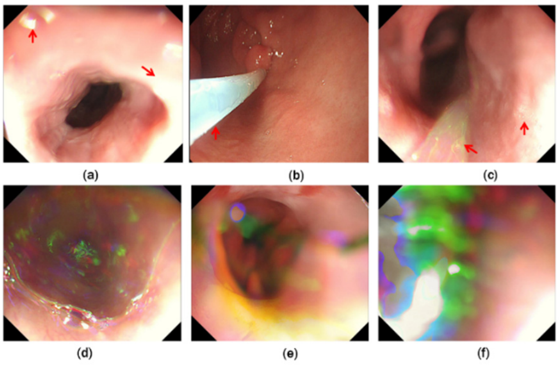

Figure 2: Examples of frames with artefacts (arrow). (a) saturation; (b) instrument; (c) bubbles; (d)(e)(f) colour misalignment (all over images).

of artefacts (red arrows) still contains visible GI features but bottom row of colour misalignment (whole images) mis-represents GI contents.

To detect artefacts, many deep learning-based systems are developed offering promising performance (Ali 2020, Ali 2021b, Bissoonauth-Daiboo 2023). In this study, the processing time also plays an important role for the future development of real-time 3D systems. Hence the real-time system, real-time instance segmentation system, YOLACT (Bolya 2019, Gao 2023) is enhanced and applied for artefact classification. Figure 2 presents the architecture of the network to classify frames with normal or artefact features (instrument, bubbles, saturation or colour misalignment (CMA)). In this pre-processing stage, only frames with CMA will be discarded. This is because the subsequent 3D modelling and reconstruction of lesioned GI depends on the information of colour and intensity attributes, i.e. structure from motion and neutral radiance fields.

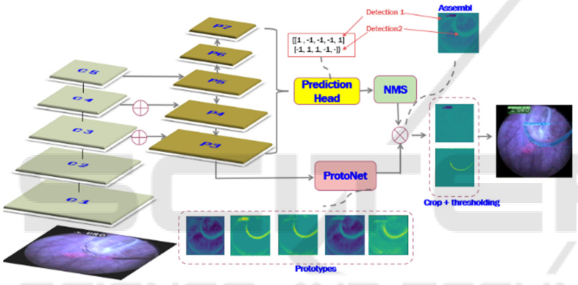

Figure 3: The architecture of YOLACT network for detection and segmentation of artefact. The artefacts to distinguish are instrument, bubbles, saturation, and colour misalignment (CMA). The mask or ground truth of frames with CMA is the whole frame.

For this end-to-end detection system of YOLACT (Bolya 2019) (Figure 3), the basic underline model employs ResNet101 to extract initial feature maps. The object segmentation is accomplished through two parallel subnets (*ProtoNet* and *Prediction Head*), which generate a set of prototype masks and predict per-object mask coefficients respectively.

More specifically, ProtoNet employs a fully connected network (FCN) accommodating the largest pyramid feature layer ($P3$), to produce a set of image-sized *prototype masks*. These k mask prototypes ($k = 32$ in this study) are then applied to deliver predictions for the entire image in relation to classification, segmentation and detection (Gao 2023).

On the other hand, Prediction Head contains three branches, which are *c class confidence (c=5 for 'Instrument', 'Bubbles', 'Saturation', 'artefact-text', 'CMA')*, *4 bounding box regressors (=[x$_{top\text{-}left\text{-}corner}$, y$_{top\text{-}left\text{-}corner}$, width, height])), and* a vector of mask coefficients, one for each prototype to be processed in parallel. Subsequently, the branch of '*Crop+thresholding*' in Figure 2 delivers a vector size of $4 + c + k$ for each anchor or region of interest (RoI), As a result, for each instance, one or more masks will stem from that instance by linearly combining (plus or minus) the work from both *prototype and mask coefficient* strands, leading to the production of final masks (M) by a sigmoid nonlinearity as formulated in Eq. (1).

$$M = \sigma(PC^T) \tag{1}$$

where P is an $h \times w \times k$ matrix of prototype masks and C is a $n \times k$ matrix of mask coefficients for n instances that have passed *score thresholding* and initial NMS, the maxima suppression technique (Bolya 2019). NMS determines whether an instance should be kept or discard. For example, duplicated detections are suppressed not only for the same class but also for cross-class boundary boxes depending on the probability of boxes, i.e. the box with higher probability suppresses the one with lower probability. In Eq. (1), C^T indicates the transpose of C Matrix.

The calculation of the loss function is the same as for YOLACT (Bolya 2019). Three loss functions are utilised to train this end-to-end detection model as formulated in Eq. (2), which are classification loss ($\mathcal{L}_{class}$), box regression loss ($\mathcal{L}_{box}$) and mask loss ($\mathcal{L}_{mask}$) where the weights of 1, 1.5, and 1.5 are applied for them respectively to give more weight to classification.

$$\mathcal{L} = \mathcal{L}_{class} + 1.5\,\mathcal{L}_{box} + 1.5\,\mathcal{L}_{mask} \tag{2}$$

In particular,

$$\mathcal{L}_{mask} = BCE(M, M_{gt}) \tag{3}$$

where the binary cross entropy BCE is formulated using Eq. (4).

$$BCE(p,y) = -\frac{1}{N}\sum_{i=1}^{N}[y_i \log(p_i) + (1-y_i)\log(1-p_i)] \tag{4}$$

where y represents the label and p is the predicted probability of the point being a label for all N points. M and M_{gt} are calculated in Eq. (1).

After removing the frames with CMA artefact, the remaining are applied to train the 3D model takes place based on NeRF.

2.2 3D View Reconstruction for Concerned Lesioned GI Based on NeRF

For 3D scene modelling, neural radiance fields (NeRFs) (Mildenhall 2020) takes 5-degree coordinates as an input. The 5D refer to each 3D point at (x, y, z) when viewing with a camera ray of light emitting direction at (θ, ϕ). Hence, NeRF enables learning novel view synthesis, scene geometry and reflectance properties by optimising a deep fully-connected neural network as a multilayer perceptron (MLP). As such, NeRF represents this 5D function by regressing from a single 5D coordinate (x, y, z, θ, ϕ) to a single volume density and view-dependent RGB colour. As a result, to render NeRF from a specific viewpoint, camera rays are marched through the scene, and a neural network produces colours and densities for 3D points, which are then accumulated into a 2D image.

Figure 4 schematically illustrates the process of representing scenes as neural radiance fields for view synthesis.

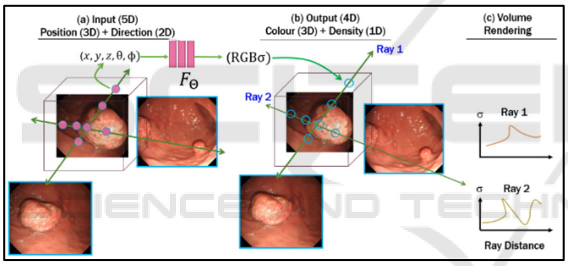

Figure 4: The process flow of NeRF. (a) 5D input; (b) 4D output; (c) volume rendering at a new viewing direction.

Firstly, a scene (Figure 4(a)) is represented using a 5D vector-valued function with an input of a 3D location $\boldsymbol{x} = (x, y, z)$ and 2D viewing direction $\boldsymbol{d} = (\theta, \phi)$. The output of this function is an emitted colour $\boldsymbol{c} = (r, g, b)$ and volume density $\boldsymbol{\sigma}$ (Figure 4(b)) at each ray. This 5D function is approximated applying a multilayer perceptron (MLP) network $F_\Theta: (\boldsymbol{x}, \boldsymbol{d}) \rightarrow (\boldsymbol{c}, \boldsymbol{\sigma})$ to optimise its weights $\boldsymbol{\Theta}$ in order to map each input 5D coordinate to its corresponding volume density and directional emitted colour. Finally, based on the classical volume rendering approach (Kajiya 1984), the colour of any light ray passing through the scene is rendered (Figure 4(c)) whereas the volume density $\boldsymbol{\sigma}(\boldsymbol{x})$ is interpreted as the differential probability of a ray terminating at location $\boldsymbol{x}$. Hence the expected colour $C(\boldsymbol{r})$ of camera ray light $\boldsymbol{r}(t) = \boldsymbol{o} + t\boldsymbol{d}$, starting at the original location $\boldsymbol{o}$, with near and far bounds t_n and t_f , is expressed in Eq. (5) (Mildenhall 2020).

$$C(r) = \int_{t_n}^{t_f} T(t)\sigma(\boldsymbol{r}(t))c(\boldsymbol{r}(t), \boldsymbol{d})dt \qquad (5)$$

where

$$T(t) = \exp\left(-\int_{t_n}^{t} \sigma(\boldsymbol{r}(s))ds\right) \qquad (6)$$

As pointed out by Mildenhall et al [6], operating a network F_Θ directly on $xyz\theta\phi$ can result in poorly rendering performance when colour and geometry have high-frequency variations. Hence, F_Θ is formulated as a composite of two functions, i.e., $F_\Theta = F'_\Theta \circ \gamma$, where F'_Θ is learned applying a regular MLP network, from which the estimated colour $\hat{C}_c(\boldsymbol{r})$ can be expressed in Eq. (7) as a weighted sum of all sampled colours c_i along the ray.

$$\hat{C}_c(\boldsymbol{r}) = \sum_{i=1}^{N_c} w_i c_i \qquad (7)$$

where

$$w_i = T_i(1 - \exp(-\sigma_i \delta_i)) \qquad (8)$$

$$T_i = \exp\left(-\sum_{j=1}^{i-1} \sigma_j \delta_j\right) \qquad (9)$$

and

$$\delta_i = t_{i+1} - t_i \qquad (10)$$

δ_i in Eq (10) refers to the distance between adjacent samples.

On the other hand, γ is not learnt but a mapping from $\mathbb{R}$ space into a higher dimensional space $\mathbb{R}^{2L}$ as computed in Eq. (11).

$$\gamma(p) = (\sin(2^0\pi p), \cos(2^0\pi p), \dots, \sin(2^{L-1}\pi p), \cos(2^{L-1}\pi p)) \qquad (11)$$

Where $p = x, y, z, \theta, \phi$ respectively. $L = 10$ when $p = x, y, z, \theta, \phi$ and $L = 4$ when $p = \theta, \phi$.

Hence the loss between ground true colour $C(\boldsymbol{r})$ and predicted pixel colours for both coarse $\hat{C}_c(\boldsymbol{r})$ and fine $\hat{C}_f(\boldsymbol{r})$ renderings is calculated in Eq. (12).

$$\mathcal{L} = \sum_{r\in\mathcal{R}}\left[\left\|\hat{C}_c(\boldsymbol{r}) - C(\boldsymbol{r})\right\|_2^2 + \left\|\hat{C}_f(\boldsymbol{r}) - C(\boldsymbol{r})\right\|_2^2\right] \qquad (12)$$

where $\mathcal{R}$ is the set of rays in each batch.

2.3 Implementation

To model 3D view of endoscopic view based on NeRFs, Nerfstudio (Tancik 2023) is implemented. Nerfstudio tools are a repository collecting an family of simple python-based extensive application programing interface (API) functions to allow visualisation of modelling of scenes based on neural radiance fields

(NeRFs). By providing a simplified end-to-end process of creating, training and testing NeRFs, these APIs allow viewing and interacting these processes through an internet browser.

In this study, the input data are a clip of endoscopic video containing RGB frames. After removal of artefact of CMA as explained in Section A, these frames/images are analysed to extract needed information, including ground truth information such as camera intrinsic and extrinsic data. To obtain the endoscopic camera information, COLMAP system is employed. COLMAP (Schonberger 2016) is the structure-from-motion (SfM) package that can be employed to estimate the ground truth information regarding to camera poses, camera intrinsic parameters, and scene boundaries. In addition, this pre-processing stage converts those input images into a format that is compatible with NerfStudio [1], i.e. a JSON format.

Then training takes place based on the pre-processed images to create a configuration file and a model.

2.4 Similarity Measurements

Three common measures are employed to calculate the similarity between original (ground truth) and rendered images, which are structural similarity (SSIM) (Wang 2004) (Eq. (13)), peak signal-to-noise ratio (PSNR) (Eq. (14)), and more recently Learned Perceptual Image Patch Similarity (LPIPS) (Eq.(15)).

$$SSIM(x,y)=\frac{(2\mu_x\mu_y+c_1)(2\sigma_{x,y}+c_2)}{(\mu_x^2+\mu_y^2+c_1)(\sigma_x^2+\sigma_y^2+c_2)} \quad (13)$$

In Eq. (13) of SSIM, μ_x, μ_y are the averages of x, y, with σ_x^2, σ_y^2 being the variances of x, y respectively and $\sigma_{x,y}$ the covariance of x and y. The variables of c_1 and c_2 are applied to stabilize the division when a small denominator occurs and are set to be $(0.01L)^2$ and $(0.03L)^2$ respectively, whereby L stands for the dynamic intensity range of an image, e.g. L=255 for an 8-bit image. x, y refer to original and rendered images respectively.

For PSNR, Eq. (14) is calculated.

$$PSNR=20\log_{10}MAX_I-10\log_{10}MSE \quad (14)$$

where MAX_I refers to the maximum possible value of the image (e.g. 255 for 8-bit) and MSE the mean squared error between two concerned images.

In addition, LPIPS (Zhang 2018) metric refers to Learned Perceptual Image Patch Similarity and is formulated in Eq. (15). LPIPS is calculated by comparing the activations of two image patches using pre-defined neural network features. Specifically, it computes the distance between the feature representations of the patches. The lower the LPIPS score is, the more perceptually similar the patches are. The distance between reference and rendered patches x, x_0 with network $\mathcal{F}$ is calculated in Eq. (15) where H, W, C refer to image patch high, width, and channel.

$$d(x,x_0)=\sum_l\frac{1}{H_lW_l}\sum_{h,w}\left\|w_l\odot(\hat{y}_{hw}^l-\hat{y_0}_{hw}^l)\right\|_2^2 \quad (15)$$

The feature stacks are extracted from layer L where unit-normalization ($\hat{y}$, $\hat{y_0}$ corresponding to x, x_0 respectively) in the channel dimension takes place, and for layer l, $\hat{y}^l$, $\hat{y_0}^l\in\mathbb{R}^{H_l\times W_l\times C_l}$. The weight w_l is performing element-wise multiplication ($\odot$), which is equivalent to computing cosine distance (Zhang 2018).

3 RESULTS

Figure 5 demonstrates the training processing implemented via Nerfstudio. The training processing is visualised live on a browser, which allows users to select any camera ray direction as exemplified at Figure 5 (a)(b) to view detailed training (5(a)) as well as each individual training image (5(b)) with a specific camera location (Figure 5(c)).

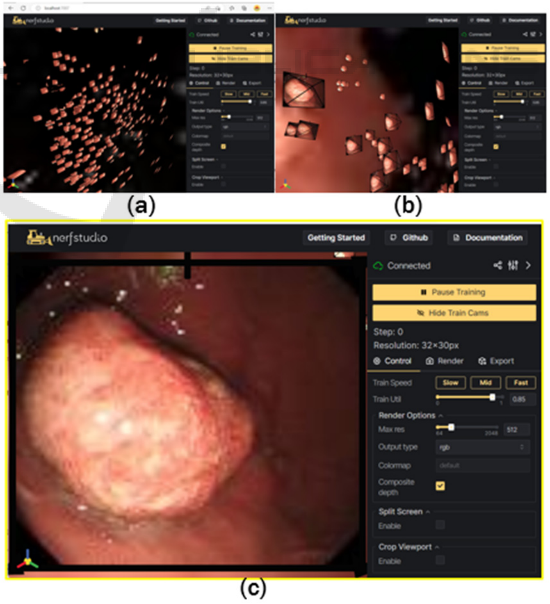

Step: 0
Resolution: 32×30px
Train Util: 0.85
Max res: 512
Output type: rgb
Colormap: default
Composite depth: ☑
Split Screen Enable: ☐
Crop Viewport Enable: ☐

Figure 5: The illustration of training process. (a)(b) training takes place at varying camera rays. (c) An individual training sample selected from (b) with a specific camera ray direction.

[1] https://docs.nerf.studio.

Figure 6 demonstrates the montage of training data set (a) and the new view angle (b) rendered using the trained model. The needed view path can be selected, defined or requested through the visualisation tool presented in Figure 5.

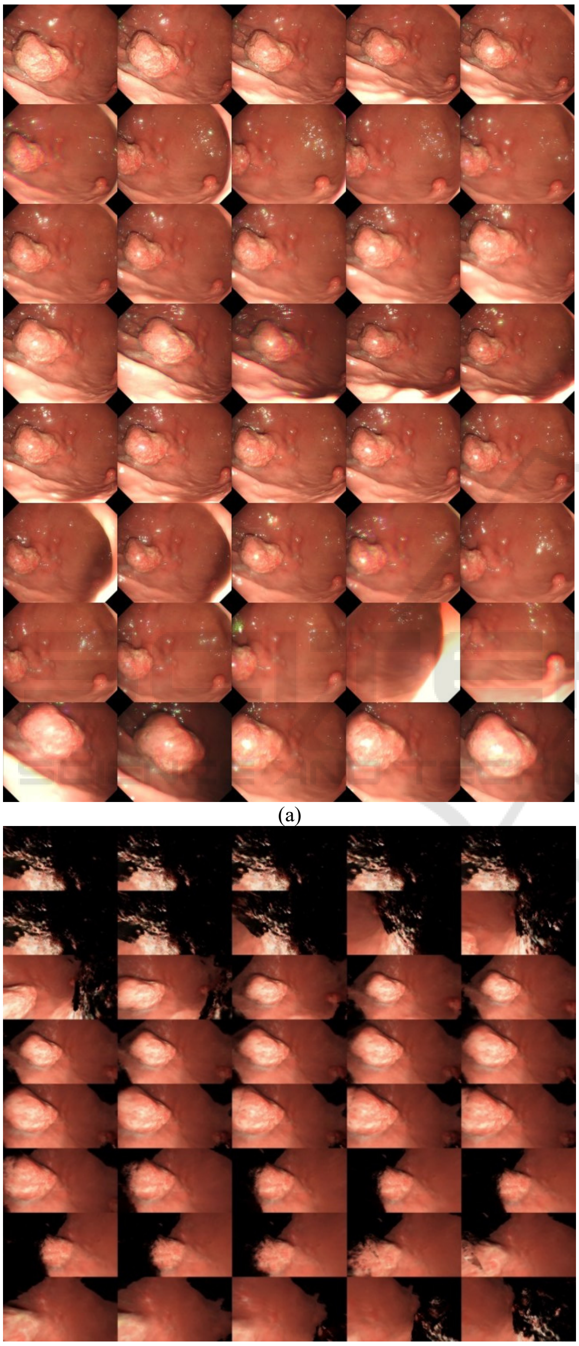
(a)

(b)

Figure 6: Demonstration of training data (a) and rendered data (b) at a specific view direction for a polyps in the stomach.

While the rendered data (Figure 6(b)) have some background information missing due to the lack the sufficient data, the concerned lesion can be rendered and viewed at any needed viewing angle, which is important in a clinical setting as an endoscopic camera can only travel in one direction within the narrow food path whereas clinicians need to know all the surrounding information for a surgical planning.

The accuracy of rendered images using the aforementioned three metric measures is provided in Table 1, which is based on two sets of data. The initial video frames with 10 minutes each contains over 30,000 frames each. After pre-process for detection of colour misalignment artefact, 6000 frames are kept. When extracting camera ray information using COLMAN approach, only 2600 images are found related due to poor image quality, e.g. blurry with floating objects or noise/artefact.

Table 1: The measurement of similarity between ground truth (original) and rendered images. for psnr and ssim, higher value implies more similar whereas lower lpips referring more similar between the two.

Data set	Image number	PSNR	SSIM		LPIPS
2	2600	19.46 ± 2.56	0.70 ± 0.054		0.49 ± 0.05

Figure 7 presents a mesh and point cloud for the concerned lesion shown in Figure 5, which can be views at any viewing angle or camera light ray.

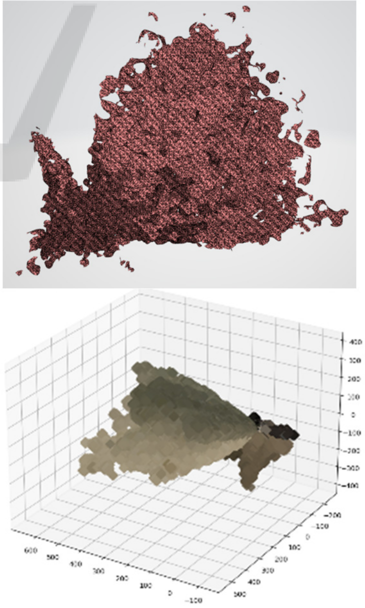

Figure 7: Demonstration of mesh (top) and point cloud (bottom) of the concerned lesion shown in Figure 5.

4 CONCLUSION

This study investigates the feasibility of reconstruction of 3D scene of GI from 2D endoscopic videos as an end-to-end process, i.e. from an input 2D video to an output 3D model, without the prior knowledge of camera information of location, intrinsic and extrinsic data. SOTA NeRF approach is applied. Because of the challenges facing acquisition of endoscopic video with less texture information on the GI surface, the camera positional information extracted from videos requires images with varying view angles, which in our case, is limited. Hence the ground truth images after pre-processing only contain 10% of the original input. However, even with only 1000 images for each lesion as one training dataset, the 3D model is able to render high quality images with various viewing angles. For the two training data sets, the averaged measures of SSIM, PSNR and LPIPS between original (ground truth) and rendered images are 19.46 ± 2.56, 0.70 ± 0.054, and 0.49 ± 0.05 respectively. In comparison with the work of NeRF where 31.01, 0.947 and 0.081 are obtained for natural images [6], our results appear to be less performed. However, in [6], around 100 views are acquired for each filmed object with known camera information. In our study, this information has to be extracted from endoscopic videos themselves with much less viewing angles due to the constraints of viewing space in the food passage, leading to less image frames are employed. In addition, because of the combination of movements while performing endoscopic filming, including heartbeat, respiration, and camera, many images appear blurry to a certain extent. These blurry images are usually ignored when applying COLMAP library to track camera locations. This is because the tracking of motion based on optical flow, i.e. the same spot would appear similar intensity level in the subsequent images, which is not the case for blurry images.

In the future, more datasets will be evaluated. In addition, post processing will be conducted including to remove noises or ghostly artefact as recommended more recently by Warburg et al (Warburg 2023). Specifically, to make use as many video frames as possible, especially for medical applications with limited dataset, a new algorithm will be developed to establish camera information based on the existing available but less clear images through the application of human vision models. While many frames are burry with regard to motion tracking, human vision can still perceive these motions easily and clearly. In this way, the developed system will also become more transparent.

ACKNOWLEDGEMENTS

This project is founded by the British Council as Women in STEM Fellowship (2023-2024). Their financial support is greatly acknowledged.

REFERENCES

Ali S, Zhou F, Braden B, et al (2020), “An objective comparison of detection and segmentation algorithms for artefacts in clinical endoscopy,” Nature Scientific Reports, 10, Article number: 2748.

Ali S, Bailey A, Ash S, et al. (2021a), “A Pilot Study on Automatic Three-Dimensional Quantification of Barrett’s Esophagus for Risk Stratification and Therapy Monitoring”, Gastroenterology, 161: 865-878.

Ali S, Dmitrieva M, Ghatwary N, et al (2021b), “Deep learning for detection and segmentation of artefact and disease instances in gastrointestinal endoscopy,” Medical Image Analysis, 70:102002.

Bae G, Budvytis I, Yeung CK, Cipolla R (2020), “Deep Multi-view Stereo for Dense 3D Reconstruction from Monocular Endoscopic Video”, MICCAI 2020. Lecture Notes in Computer Science, vol 12263. Springer.

Bissoonauth-Daiboo P, Khan MHM, Auzine MM, Baichoo S, Gao XW, Heetun Z (2023), “Endoscopic Image classification with Vision Transformers,” in ICAAI 2023, pp. 128-132.

Bolya D, Zhou C, Xiao F, Lee YJ (2019), YOLACT: real-time Instance Segmentation, Proceedings of the ICCV 2019.

Gao XW, Taylor S, Pang W, Hui R , Lu X, Braden B (2023), “Fusion of colour contrasted images for early detection of oesophageal squamous cell dysplasia from endoscopic videos in real time , Information Fusion,” 92: 64-79.

Kajiya JT, Herzen BPV (1984), “Ray tracing volume densities,” Computer Graphics, SIGGRAPH.

Lu L, Mullins CS, Schafmayer C, Zeißig S, Linnebacher M (2021), “A global assessment of recent trends in gastrointestinal cancer and lifestyle-associated risk factors,” Cancer Commun (Lond), 41(11): 1137-1151.

Mildenhall B, Srinivasan PP, Tancik M, et al. (2020), NeRF: Representing Scenes as Neural Radiance Fields for View Synthesis, in ECCV 2020.

Prinzen M, Trost J, Bergen T, Nowack S, Wittenberg T (2015), “3D Shape Reconstruction of the Esophagus from Gastroscopic Video,” In: H Handels, et al. (eds) Image Processing for Medicine, pp. 173-178. Springer Berlin, Heidelberg.

Schonberger JL, Frahm JM (2016), “Structure-from-motion revisited,” In: CVPR’2016.

Tancik M, Weber E, Ng E, et al (2023), Nerfstudio: a Modular Framework for Neural Radiance Field Development, arXiv:2302.04264.

Wang Z, Bovik AC, Sheikh HR, Simoncelli EP (2004), “Image quality assessment: From error visibility to structural similarity," IEEE Transactions on Image Processing, 13 (4) : 600-612.

Warburg F, Weber E, Tancik M, Hołyński A, Kanazawa A (2023)," Nerfbusters: Removing Ghostly Artifacts from Casually Captured NeRFs," ICCV'2023.

Widya A, Monno Y, Imahori K, et al (2019), "3D reconstructor of whole stomach from endoscope video using structure-from-motion", arXiv:1905,12988v1.

Zhang R, Isola P, Efros AA, Shechtman E, Wang O (2018), "The unreasonable effectiveness of deep features as a perceptual metric," In: CVPR'2018.